Article

Not peer-reviewed version

Cellular Patterns of the Skin Microenvironment in Experimentally Induced Diabetes Mellitus

Doinița Temelie-Olinici , Ionuț-Cătălin Botezatu * , Mihaela Perțea * , Laura Stoica , Pavel Onofrei , Ana-Emanuela Botez , Vasile-Bogdan Grecu , Raluca Maria Haba , Petronela Bărgăoanu , Carmen Elena Cotrutz

Posted Date: 28 June 2023

doi: 10.20944/preprints202306.2059.v1

Keywords: streptozotocin diabetes; ultrastructural diagnosis; insulin resistance.

Article

Changes in Snow Surface Albedo and Radiative Forcing in the Chilean Central Andes Measured by In-Situ and Remote Sensing Data

Luis Figueroa-Villanueva [1,2,*], Lina Castro [1,2,*], Tomás R. Bolaño-Ortiz [2], Raúl P. Flores [1,2], Diego Pacheco [1,2] and Francisco Cereceda-Balic [2,3]

[1] Departamento de Obras Civiles, Universidad Técnica Federico Santa María, Valparaíso 2340000, Chile
[2] Centre for Environmental Technologies (CETAM), Universidad Técnica Federico Santa María, Valparaíso 2340000, Chile
[3] Departamento de Química, Universidad Técnica Federico Santa María, Valparaíso 2340000, Chile
* Correspondence: luis.figueroav@alumnos.usm.cl (L.F.-V.); lina.castro@usm.cl (L.C.)

Abstract: Snow-covered regions are the main source of reflection of incident shortwave radiation (ISR) on Earth's surface. The deposition of light-absorbing particles (LAPs) on these regions increases the capacity of snow to absorb ISR and decreases surface snow albedo (SSA), which intensifies the radiative forcing leading to accelerated snowmelt and modifications of the hydrologic cycle. In this work we investigate changes in SSA and radiative forcing (RF) induced by LAPs in the Upper Aconcagua River Basin (Chilean central Andes) using remote sensing satellite data (MODIS), in-situ spectral SSA measurements, and the ISR (Chilean Solar Explorer platform) during the austral-winter months (May to August) for the 2004-2016 period. To estimate the changes in SSA and RF, we define two spectral ranges: i) an enclosed range (Ecr) between 841-876 nm, which isolates effects of Black-Carbon, an important LAP derived from anthropogenic activities, and ii) a broadband range (Bbr) between 300-2500 nm. Our results show that percent variations in SSA in the Ecr are higher than in the Bbr, regardless of the total amount of radiation received, which may be attributed to the presence of LAPs as these particles have a greater impact on SSA at wavelengths in the Ecr band than in the Bbr band.

Keywords: snow surface albedo; Radiative Forcing; light-absorbing particles in snow; remote sensing; Black Carbon; Chilean Central Andes Mountains

1. Introduction

Uncontaminated snow surfaces are among the whitest surfaces on Earth and have one of highest broadband albedos in the solar spectrum range [1]. Surface snow albedo (SSA) is a fundamental factor for the reflection of incident shortwave radiation (ISR) in the global snow-atmosphere budget system [2–5]. In the visible (VIS) and near-infrared (NIR) spectral ranges (<1μm), SSA is strongly influenced by the presence of light-absorbing particles (LAPs), whereas for wavelengths above 1μm the variability of SSA is mainly controlled by the grain size of snow crystals [6,7]. The deposition of LAPs in snow darkens the surface of the snowpack, decreasing the reflection of ISR and the albedo [8–10]. Moreover, grain metamorphism is accelerated in the presence of LAPs, through a process that is typically referred to as the snow-grain-size feedback, [11,12], which results in a higher ISR absorbing capacity [13,14]. Consequently, LAPs increase the radiative forcing (RF) with the potential to accelerate snowmelt and disturb the hydrologic cycle in snow-dominated basins [15]. The deposition of LAPs in snow has also been observed to contribute to regional warming [16].

Several studies have documented the reduction of SSA due to LAPs such as Black Carbon, Brown Carbon and Mineral Dust, and the effects on local hydrological processes [12,13,17–19]. Black Carbon (BC), also known as soot [20], is an aerosol generated from the incomplete combustion of fossil fuels, biofuels, and biomass [11,21]. In Asia, BC emissions were found to be a significant precursor of glacier melting in the Himalayas [19], the Tibetan Plateau [22] and regions in Northern China [23]. Brown Carbon (BrC) is an organic carbon (OC) fraction, primarily emitted by the incomplete combustion of biomass or by the oxidation of anthropogenic and biogenic gaseous precursors [24]. The effect of BrC is comparable to the snow darkening effect of black carbon, ranging from around half to the same darkening of snow surfaces as soot [25]. Mineral dust is transported to snow-covered areas from arid regions or from anthropogenic sources like opencast mining and the construction industry [26,27]. In the Upper Colorado River Basin, heavy dust loads deposited on snow due to industrial and urban expansion resulted in a shift of the timing of peak snow-melt driven runoff and an increase in evapotranspiration as vegetation was exposed earlier [28]. Observations also suggest that Saharan dust anticipates the snowmelt which implies a shorter winter season in the European Alps [29] altering its hydrological response.

Research along the Chilean central Andes has primarily focused on the reduction of snow albedo by BC [27,30,31]. Since obtaining field measurements in high mountain environments is a difficult task, studies have mainly included point measurements of SSA that do not account for the spatial variability of the complex climatic and topographic conditions of the Chilean Andes [32,33]. The lack of knowledge of the spatial variability of SSA and the distribution of LAPs over the Andes renders albedo estimations for hydrological modelling to empirical parameters, which increases uncertainties in runoff predictions and does not consider the environmental impacts driven by the deposition of these particles. In this context, remote sensing tools emerge as a valuable tool as they provide data at high spatio-temporal resolution for monitoring snow covered regions at high elevations [34], offering promising opportunities to improve the assessment, observation, and modeling of snow processes [1,35,36].

This study aims to evaluate changes in RF associated with the presence of BC, which is emitted by anthropogenic activities such vehicular traffic and the mining industry that occur in the Andes [37]. We separate the solar spectrum into a broadband (Bbr) and enclose (Ecr) ranges to isolate the impact of BC [38]. The broadband range considers wavelengths of 300-2500 nm, while the enclose range considers a narrower band with wavelengths between 841-876 nm. We use observations from the Moderate Resolution Imaging Spectroradiometer (MODIS) and modeled ISR from the Chilean Solar Explorer (SE) to evaluate temporal and spatial changes in RF, which are validated against in-situ SSA and ISR measurements collected in the Upper Aconcagua River Basin (UARB) in the Chilean central Andes. The MODIS Dust Radiative Forcing in Snow (MODDRFS) [39,40] product was used to estimate the continuous and integrated daily RF for each spectral range, which are analyzed for temporal trends and variability throughout the 2004-2016 period. The paper is organized as follows: Section 2 describes material and methods, and Section 3 presents the results and discussion. Finally, conclusions are presented in Section 4.

2. Materials and Methods

2.1. Study Area

Central Chile is characterized by a Mediterranean climate, with mild-wet winters and dry summers [41]. Precipitation occurs during the austral winter due to sporadic cold fronts, and orographic effects may produce very localized rainfall patterns [42]. Since 2010 the central Chile region has experienced a so-call mega-drought, characterized by a series of dry years that typically show a 25% to 45% deficit in annual precipitation [43]. Several studies have reported significant decreases in snow cover duration and extent [34,44] and significant losses in glacier mass [45] over the last decade.

The study area corresponds to the Upper Aconcagua River Basin (UARB) in the Chilean Central Andes (Figure 1). The watershed is located in the Valparaíso district approximately 80 km northeast of Santiago, Chile's largest city and capital. The UARB extends between 32°15′–33°15′S and 70°0′–70°45′W, with an area of approximately 3,660 km^2 and elevations ranging from 800 to 6,000 meters above sea level (m.a.s.l.). Mean watershed altitude is approximately 3,000 m.a.s.l. The UARB includes four meteorological stations, which are managed by the Dirección General de Aguas (DGA), and provide daily precipitation and temperature data (Resguardo Los Patos, Riecillos, and Vilcuya) and snow depth (Portillo, see Figure 1). A laboratory-refuge, managed by the Centre for Environmental

Technologies (CETAM) of Universidad Técnica Federico Santa María (USM), named NUNATAK-1 (NNTK-1) (32°50’43’’S, 70°07’47’’W and 2,813 m.a.s.l.), measures atmospheric variables such as incident and reflected radiation (shortwave and longwave), air quality (aerosols and gases) and meteorology, including snow height since 2016. Monthly mean temperature in the UARB typically oscillates between 9.7°C to 10.9°C and 19.6°C to 21.1°C during the austral winter and summer, respectively, with an annual mean of 15.2°C. Mean annual precipitation is 360 mm, with approximately 280 mm occurring in fall-winter seasons (May to August). Maximum snow depth occurs in July or August, with values typically exceeding 1,700 mm (snow water equivalent of 813 mm) and a historical maximum of 2,590 mm in August 1997 (snow water equivalent of 1,201 mm).

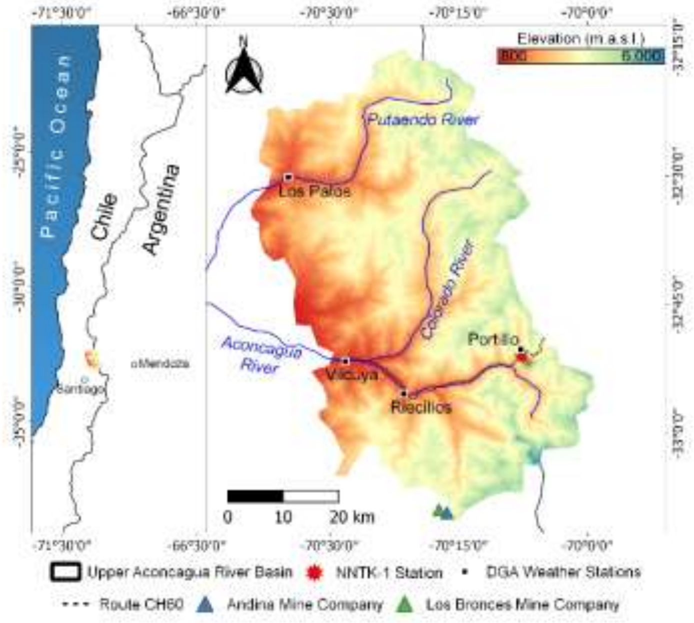

Figure 1. (**a**) Location of the Chilean central Andes, (**b**) Study Area (UARB), indicating the location of meteorological stations, mining activities, and main traffic route (CH60). Color scale denotes terrain elevation (meters above sea level).

2.2. Database

2.2.1. NUNATAK-1 laboratory-refuge

NUNATAK-1 (NNTK-1) is a laboratory-refuge located at an altitude of 3,000 m.a.s.l. (Figure 1) located within the winter quarters of the Mountain School of the Chilean Army in Portillo, border crossing between Chile and Argentina. Its main purpose is to study environmental pollution and atmosphere-cryosphere interactions, specifically how air pollution affects the melting of glaciers and climate change [32,46]. NNTK-1 measures variables such as concentration and size distribution of aerosol, atmospheric concentrations of BC and BrC, and net solar irradiance. A portable Kipp & Zonen 4-Component Net Radiometer (CNR4) is used to measure incoming and reflected solar irradiances and estimate surface snow albedo. The radiometer includes a pyranometer, with a sensitivity of 10-20 $\mu VW^{-1}m^{-2}$ and maximum uncertainty of 5% (95% confidence level), which covers the solar spectrum in the 300 to 2,800 nm range. The instrument registers the incident and reflected radiation at 1-minute frequency. For this study, we only used information from the pyranometer for the 2016-2019 period, which was available at the time of data processing. The in-situ surface snow albedo ($SSA_{in\ situ}$) was calculated for the 300-2,800 nm range, as follows:

$$SSA_{in\ situ} = \frac{R_r}{R_i} \quad (1)$$

where R_r and R_i correspond to the reflected and incident radiation, respectively. The ISR and SSA data collected at a frequency of 1 min were aggregated at a daily timescale (only considering daylight hours) with the purpose of comparing them to those obtained from the SE and MODIS. The in-situ SSA data was filtered to: (i) eliminate data recorded before sunrise and after sunset, (ii) discard spurious measurements caused by sensor obstruction and (iii) discard data from days with incomplete records.

2.2.2. MODIS data processing

The Moderate Resolution Imaging Spectroradiometer (MODIS) is one of the main instruments of the NASA Earth Observing System (EOS) and operates onboard the Terra and Aqua satellites, with records starting in 2000 and extending until the present [47]. The MODIS-Aqua (MYD10A1) and MODIS-Terra (MOD10A1) provide daily and complementary observations of the Earth, passing over our study area approximately at 10 AM and 2 PM (local time, GMT-3), respectively.

We used the reflectance data from band 2 (841-876 nm) from the Surface Reflectance Daily L2G Global 500m SIN Grid, V6 product (M*D09GA) to assess the level of absorption of incident shortwave radiation (ISR) in the range where the effects of BC are maximized (~880 nm) [38,48]. The SSA in a broadband spectral range for snow (300 to 2,500 nm) was obtained from the Snow Cover Daily L3 Global 500m SIN Grid, V6 product (M*D10A1) [47]. Each data pixel has an indicator for the quality of the measurement (QA), which is used to filter the data. Data is used only if the QA indicates the best quality (QA=0) or good quality (QA=1), as a criterion to increase the accuracy of radiative forcing estimations from satellite imagery and reduce the uncertainties in the process [39,40]. For validation purposes, data is extracted from the pixel containing NNTK-1 and compared to the in-situ measurements (see Section 2.2.1).

2.2.3. Solar Explorer

The Solar Explorer (SE) (http://solar.minenergia.cl/exploracion) is a tool developed by Chilean Energy Ministry to calculate the photovoltaic potential in the Chilean territory [49]. The model calculates the shortwave radiation at the top of the atmosphere (RTOA) and at surface level including ISR and longwave radiation for the 2004 to 2016 period. For these calculations the model uses the parametrization of solar radiation developed by the Goddard Climate and Radiation Branch (CLIRAD-SW) [50] in combination with information of atmosphere radiation from the TIM/SORCE satellite (Total Irradiance Monitor/Solar Radiation and Climate Experiment) [51], topographic data from the Shuttle Radar Topography Missions (SRTM) site [52,53], and the Geostationary Operational Environmental Satellite (GOES EAST) [54] for cloud detection. The ISR data have been validated against in-situ radiation data from 82 weather stations distributed throughout Chile and provides hourly RTOA and ISR with a spatial resolution of 1 km per pixel (Molina [49]). We used ISR data in our RF calculations after validation against field data from NNTK-1 (see Section 2.2.1).

2.2.4. Validation of SSA and ISR

Snow surface albedo from M*D10A1(SSA_{Bb}) and modeled ISR from the Solar Explorer were validated against in-situ SSA and ISR measurements from the NNTK-1 station prior to their use in estimating the radiative forcing. Since data were available for different periods at each platform, we could only validate MODIS SSA and ISR data for years 2016-2019 and 2016, respectively. SSA_{Bb} from the MODIS-Terra and MODIS-Aqua satellites were compared separately against $SSA_{in\text{-}situ}$, and a correlation analysis was performed on a monthly basis for the entire period.

2.3. Radiative Forcing

2.3.1. MODIS Dust Radiative Forcing in Snow (MODDRFS)

We used the MODDRFS originally developed by Painter et al. [39] and improved by Miller et al. [40] to estimate the radiative forcing (RF) over snow. This algorithm was developed to study the RF on snowpack resulting from the deposition of mineral dust in the 350-850 nm wavelength range. The instantaneous RF is obtained as follows (Miller et al. [40]):

$$RF = \int_{\lambda_o}^{\lambda} F_o(\lambda, t)\, D(\lambda) d\lambda dt \tag{2}$$

$$F_o(\lambda, t) = F_{dir,local}(\lambda, t) + F_{dif}(\lambda, t) \tag{3}$$

$$F_{dir,local} = F_{dir} \frac{\sin\theta_S * \sin s * \cos(\phi_S - \alpha) + \cos\theta_S \; \cos s}{\cos\theta_S} \tag{4}$$

$$D(\lambda) = SSA_{fresh} - SSA_{effective} \tag{5}$$

where $F_o(\lambda, t)$ represents the total ISR at a wavelength λ and at time t. The total ISR $F_o(\lambda, t)$ has a local and diffuse direct component (Equation 3), where $F_{dir,local}(\lambda, t)$ is given by direct radiation $F_{dir}(\lambda, t)$ and diffuse radiation $F_{dif}(\lambda, t)$. Direct radiation is dependent on the conditions at a particular location such as the angle of solar zenith θ_s, the angle of solar azimuth ϕ_s, slope s and orientation α of the site (Equation 4). $D(\lambda)$ corresponds to the difference between the surface snow albedo in ideal conditions, e.g., fresh or pure snow (SSA_{fresh}), and the effective surface snow albedo ($SSA_{effective}$) at a wavelength λ (Equation 5). In our case, $SSA_{effective}$ is provided by the in-situ and satellite measurements, and we estimate SSA_{fresh} using the radiative transfer model SNICAR [55]. The integration limits were defined based on the wavelength range defined for Bbr and Ecr; 300-2,500 nm for the M*D10A1 product (Bbr) and 841-876 nm for M*D09GA (Ecr). Finally, the daily integrated RF (DIRF) from sunrise to sunset is given by:

$$DIRF = \int_{sunrise}^{sunset} \int_{\lambda_o}^{\lambda} F_0(\lambda, t) D(\lambda) d\lambda dt \tag{6}$$

2.3.2. Santa Barbara DISORT Atmospheric Radiative Transfer (SBDART)

We use the Santa Barbara DISORT (Discrete Ordinate Radiative Transfer) Atmospheric Radiative Transfer (SBDART) [56–58] model to obtain indirect estimates of the fraction of radiation extracted from the SE that corresponds to the spectral bands provided by the MODIS reflectance products (M*D10A1 and M*D09GA band 2). SBDART models the radiative transfer processes in the atmosphere and Earth's surface (ISR), and requires input such as time, geographic location, atmospheric profile (tropical, mid-latitude or sub-artic) in terms of water vapor density and pressure, solar zenith (sza) and azimuth (saza), type of surface albedo, and spectral boundaries. After estimating the total radiation in the 280-4000 nm range using SBDART, we can obtain the radiation $F_o(\lambda, t)$ that corresponds to the spectral ranges of MODIS products. We find that the Ecr and Bbr ranges correspond to approximately 3% and 99%vof the total $F_0(\lambda,t)$ extracted from the SE, respectively (see **Figure A1**). These percentages show small variability throughout the day, which results primarily from changes in solar zenith and azimuth (±0.3% y ±0.1%, respectively). We also determined that values obtained at 10 AM (MODIS Terra) are close to the daily mean for both spectral ranges, with differences below 1%.

2.3.3. Snow, Ice and Aerosol Radiative Model (SNICAR)

SNICAR [55] is a radiative transfer model developed to simulate spectral snow albedo as a function of snow microstructure, stratigraphy, the content of LAPs and the surface irradiance flux [59]. For this study, SNICAR was used to estimate the fresh and clean snow albedo (SSA_{fresh}), which is required for the calculation of the radiative forcing (Equations 2 and 5). For the estimation of SSA_{fresh}, we assumed clear-sky conditions, a snow grain size of 100 µm, which corresponds to a null concentration of pollutants [1,60], and a snow density of 400 kgm^{-3}, which is representative of seasonal snow [61]. Optical ice properties were estimated based on the ice refraction index proposed by Picard et al. [62]. An optically semi-infinite and uniform snowpack (0.3 m depth) was considered for the study area [60]. SNICAR albedo simulations showed that SSA_{fresh} is mainly determined by solar position (zenith and azimuth); albedo values at 10 AM throughout the UARB vary only by 1%. Similar variations (1%) were found when computing albedo throughout the day at NNTK-1's location. These results, i.e., the small spatio-temporal variability of SSA_{fresh} throughout the study area, allow us to assume that SSA_{fresh} estimated at NNTK-1's location can be extrapolated to the entire UARB to investigate the spatial variability of the radiative forcing (see Section 3.2).

2.3.4. Estimation of SSA, D, and RF at NNTK-1

As described on Equation 6, D(λ) is required to estimate the daily integrated radiative forcing (Equation 6). In turn, the estimation of D(λ) requires the SSA and ISR associated to both spectral ranges (Bbr and Ecr). The period of study is defined between 2004-2016, which corresponds to the period where the remote sensing data overlap (MODIS and SE) and the Daily Integrated Radiative Forcing (DIRF) can be estimated. We estimated SSA, D, and DIRF for all days with clear-sky conditions using the remote sensing data extracted at the location of NNTK-1. Additionally, we estimated D for every pixel situated within the UARB for days following a precipitation event. For this, we only considered events with daily images containing more than 1000 pixels with clear-sky condition, which is equivalent to a 10% of the total watershed area. Estimates of D are obtained using Equation 5, where SSA_{fresh} is taken as a constant throughout the UARB and equal to the value computed at the location of NNTK-1.

3. Results and discussion

3.1. Data validation

MODIS products reveal excessive cloudiness in 2016, such that a comparison against in-situ SSA (NNTK-1) measurements was not possible for this year. For the 2017-2019 period, we observe that the percentage of days with clear-sky condition (valid data) in June-July did not exceed 25% of the whole MODIS data set, while for August this percentage increased to 61%. Comparing the two satellites between June and August, MOD10A1 (Terra) presented a larger number of days with clear-sky conditions, as well as a higher monthly correlation value (between 0.51-0.91), except for July 2017 and 2018 where the correlation values were lower than 0.13. During June-August, MYD10A1 (Aqua) showed correlation values ranging between 0.27-0.81, however, lower values were observed for the months of June, July, and October in year 2017 (0.02, 0.20, and 0.21, respectively). The reason for the low correlation values in these months for both satellites may be attributed to two main factors: (i) few days with useful remote sensing data due to excessive cloudiness, and (ii) days where the elevation of the snow line (zero isotherm) is relatively close to the elevation of NNTK-1, with the implication of low or partial snow coverage at NNTK-1's pixel (<70%), which underestimates SSA by more than 10%, with respect to the field measurements (see Figure A2). The Solar Explorer data had been previously validated in the study area [49]. Despite this, we computed the correlation between ISR from SE and from NNTK-1, confirming a very high correlation (>0.9) during year 2016.

3.2. Temporal analysis of SSA, D(λ) and RF during 2004-2016 period at NNTK-1

Figure 2 shows SSA values for both spectral ranges (Bbr and Ecr) for the pixel corresponding to NNTK-1. After filtering, 312 days (20% of the study period) with snow and clear-sky conditions were found. SSA exhibits a similar behavior for Bbr (**Figure 2**a) and the Ecr (**Figure 2**b), with minimum values during May that increase as the austral winter progresses. The distribution of values until the third quartile is similar for both spectral ranges, ranging between 0.12-0.35 in May, 0.25-0.67 in June, 0.50-0.70 in July, and 0.55-0.75 in August. Monthly mean values (shown as white boxes in **Figure 2)** are similar, with a maximum variation of 0.02 for the month of May.

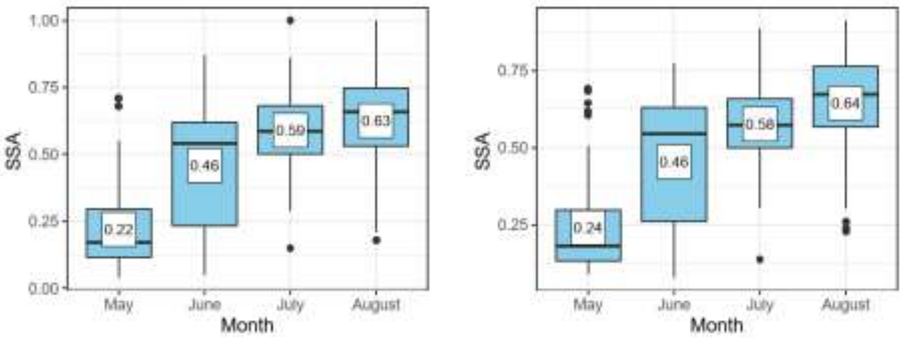

(**a**) (**b**)

Figure 2. SSA values in the Bbr (**a**) and Ecr (**b**), grouped by month in NNTK-1's location, for the 2004-2016 period. Also shows monthly mean value within white box.

To quantify the influence of LAPs on the radiative forcing, we need to compute D (Equation 5) for both spectral ranges. D values are obtained using SSA_{fresh} simulated by SNICAR during the austral winter between 2004 and 2016 considering clear-sky and the other conditions outlined in Section 2.3. We obtained daily mean values of 0.863±0.007 for the Bbr range and 0.933±0.007 for the Ecr (see Figure 3). . Figure 3 shows estimates of D for the entire study period. For each month, all DEcr values (Figure 3b) are higher than DBbr (Figure 3a), including those below quartile 3 and the monthly mean values. D_{Ecr} values within quartile 1 and 3 (above q1 and below q3) are approximately 0.07 units higher for the month of July, whereas for the other months (May, June, and August) values in the Ecr range are 0.04 units higher than Bbr. The monthly mean values of D (white boxes) in the Ecr are larger by 0.05 units for May and August (during 2004 to 2016 period) compared to those for Bbr. The monthly mean D_{Ecr} values were also higher than D_{Bbr} for June and July, with differences of 0.07 and 0.08 units respectively. We note that the differences between D_{Ecr} and D_{Bbr} increase if the analysis is made considering the daily mean values. The values of D for the Ecr were generally higher (as much as 0.25 units) than in the Bbr, with the exception of only 60 days within the 2004-2016 period (**Figure 4**).

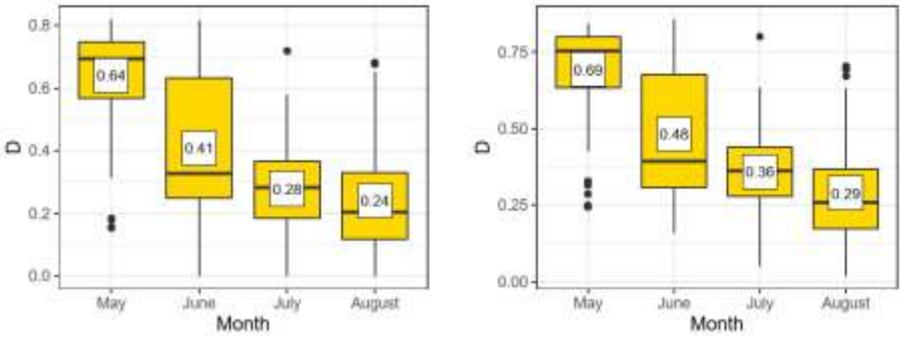

(**a**) (**b**)

Figure 3. D values in the Bbr (**a**) and Ecr (**b**), grouped by month in NNTK-1's location, for the 2004-2016 period. Also shows monthly mean value within white box.

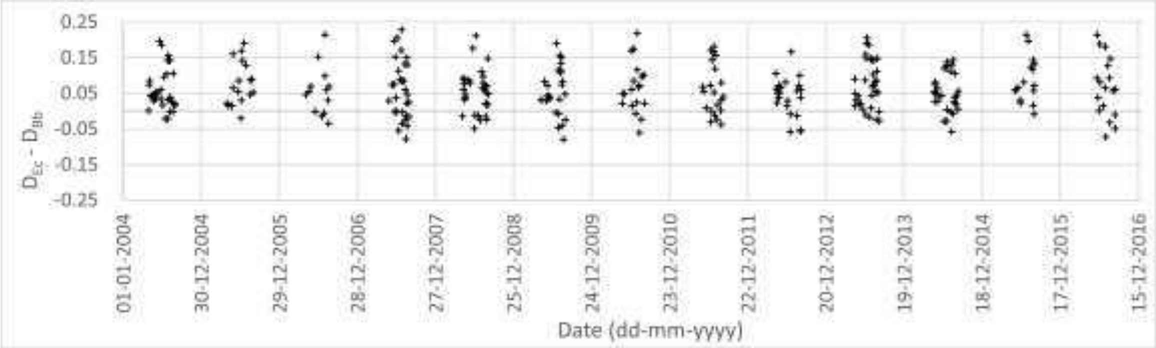

Figure 4. Difference between D in the Broadband range (Bbr) and Enclose range (Ecr) for the 2004-2016 period.

Figure 5 shows results of DIRF for the Bbr and Ecr, which are consistent with our previous results of SSA and D. DIRF reaches the higher monthly mean values (white boxes) in May, with 8.02 and 0.27 MJ m^{-2} d^{-1} for the Bbr and Ecr, respectively, and decreasing to 2.82 (Bbr) and 0.12 MJ m^{-2} d^{-1} (Ecr) in July. This scenario follows the trend observed for D between May and July (Figure 3), however, monthly mean values of DIRF in August increased to 3.58 (Bbr) and 0.13 (Ecr) MJ m^{-2} d^{-1}, whereas D continued decreasing. This difference is explained by the fact that ISR values reach minimum values during June and July, and then starts to increase (Figure A4).

In Figure 5 DIRF values reaching 13.21 MJ m-2 d-1 in the Bbr and 0.42 MJ m-2 d-1 in the Ecr. $DIRF_{Ecr}$ values are within the range reported by Rowe et al. 2019 at the same location. We note that although these authors had used a different spectral range to analyze BC effects in snow (650-700nm), the DIRF values are of the same order of magnitude (0.1-2.3 MJ m^{-2} d^{-1}). We found a maximum Instantaneous RF in the Bbr of 571.54 W m^{-2} (observed on August 29th, 2004) which is attributed to the melting of most of the snow at the corresponding pixel (snow cover value of 0.23). The instantaneous radiative forcing found in other regions around the world such as the Himalaya or across the United States, using the 350-850 nm wavelength range, are comparable with the values obtained here for the Bbr (e.g., [28]).

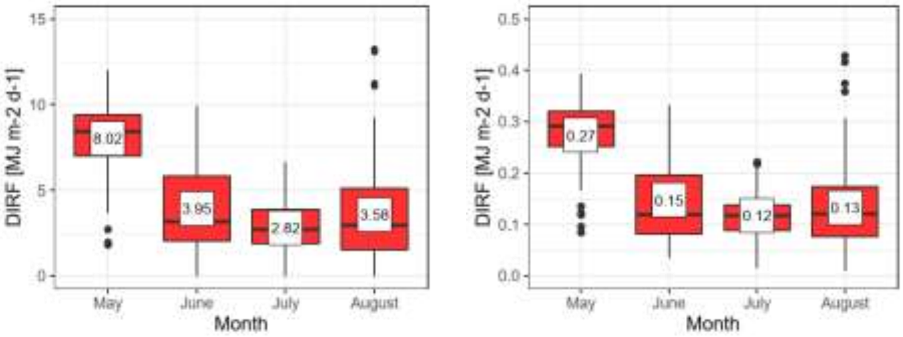

(a) **(b)**

Figure 5. DIRF values in the Bbr (**a**) and Ecr (**b**), grouped by month in NNTK-1's location, for the 2004-2016 period. Also shows monthly mean value within white box.

To compare the DIRF values between the Ecr and Bbr spectral ranges, which have different magnitudes of received radiation (3% and 99%, as shown in Section 2.3.2), we normalize the values

doi:10.20944/preprints202306.2059.v1

with respect to Bbr. This normalization allows for the determination of the percentage impact on Ecr in terms of the DIRF ($DIRF_{Ecr/Bcr}$), which can then be compared to the normalized radiation received in the Ecr range ($ISR_{Ecr/Bbr}$). From the monthly mean values in Figure 4, the normalized $DIRF_{Ecr/Bcr}$ values are 3.42%, 3.74%, 4.22%, and 3.74% for the months of May to August, respectively. Similarly, the normalized $ISR_{Ecr/Bbr}$ values are 3.17%, 3.22%, 3.23% and 3.17% for the same month, respectively. As observed, there is a difference between the $ISR_{Ecr/Bb}$ and $DIRF_{Ecr/Bcr}$ ratios for each of the months evaluated, with higher ratios observed for $DIRF_{Ecr/Bcr}$. This suggests that the variations in SSA in the Ecr are higher, and that this increase may be attributed to the presence of LAPs as these particles have a greater impact on the albedo at wavelengths between 841-876 nm (Ecr) than in the range of 300-2500 nm (Bbr), regardless of the total amount of received radiation [15,63,64].

With the purpose of following daily changes in SSA, we selected consecutive days without liquid precipitations and with equal or less snow cover after the initial day to make sure that local snowfall at Portillo did not occur (see Table 1). Figure 6 shows the variations in spectral SSA (for MODIS bands 1-4) for the periods that satisfy the former conditions throughout our study period. As expected, we observe that SSA decreases with time (from one day to the next) for most cases, which is consistent with the aging of snow and the size increase of snow grains that occur as time progresses after the storm [9,65]. For some of the selected periods, such as June 28-29th 2004 (Figure 6a), August 15-16th 2007 (Figure 6b), July 2-th 2016 (Figure 6g), and June 6-7th 2016 (Figure 6m), the spectral SSA values showed an evident decrease in the Ecr (841-876 nm) and the closest MODIS band (620-670 nm), larger than in the 459-479 nm and 545-565 nm bands. However, for the majority of days shown in Figure 6. the decrease in spectral SSA did not show much variation between bands (e.g., Figure 6c–e,h,l,m). Although there was one period where a slight increase in SSA was observed (Figure 6d), these data show a systematic decrease in spectral SSA for the visible wavelengths (MODIS bands 1-4) and particularly for the Ecr, which is usually associated to the presence of BC [19,66]. We note that the other bands in the visible wavelengths may be associated to the presence of mineral dust [39].

Error! Reference source not found. 1 shows daily SSA variations for MODIS bands 1,3 and 4, and for the Bbr and Ecr spectral ranges, as well as daily D and DIRF values for the Bbr and Ecr ranges. In general, we observe that differences between SSA for bands 1,3,4 and D (Ecr and Bbr) is approximately -0.3, with a larger difference observed for second day (see Figure 6). The maximum daily rates of albedo decrease for the Bbr and Ecr were observed in August 2013 and August 2007, respectively. These reductions in albedo seem to be much higher than values reported by previous studies in the central Andes area [32–34]. Cereceda-Balic et al. 2018 reported a reduction of 0.08 units per day in the broadband albedo (SSA_{Bbr}) resulting from the deposition of BC from vehicle emissions in the Portillo location. We attribute these differences to: i) differences in contamination sources associated to the periods and location considered in the studies, and ii) the fact that the remote sensing measurements consist of only one measurement, either at 10am or 2pm, whereas the in-situ study used continuous data from a radiometer [32].

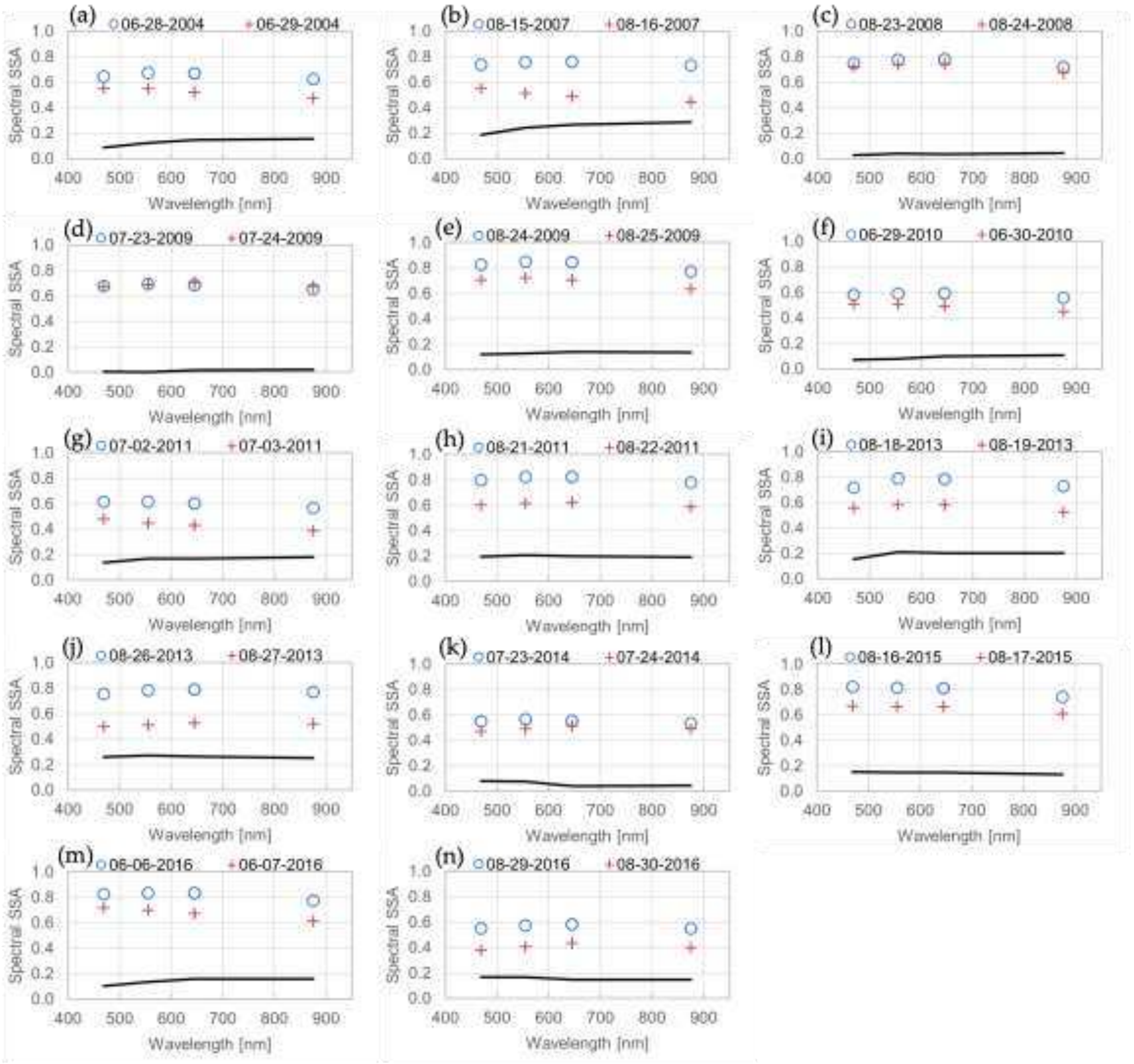

Figure 6. SSA spectral variations for MODIS bands (1-4) for 16 days. Blue circles and red crosses represent consecutive days, and the black line indicates the SSA spectral daily difference.

The results presented in Table 1 also show the differences in radiative forcing (DIRF) for the two spectral ranges of interest (Ecr and Bcr) for two consecutive days. On the second day, $DIRF_{Bbr}$ shows a 60% increase compared with the average radiative forcing of the evaluated days, whereas $DIRF_{Ecr}$ exhibited an increase of approximately 50%. When examining $DIRF_{Ecr/Bbr}$, the radiative forcing in the Ecr band represents on average a 4.46% of the radiative forcing in the Bbr band, with values reaching a 12.21% (August 18th, 2013). On the other hand, the incident solar radiation ratio $ISR_{Ecr/Bbr}$ is on average 3.18% for the days considered in Table 1, with values that reach 3.21% for June 6-7th, 2016, and 3.14% for August 18th, 2013. The above confirms previous results indicating that radiative forcing has a greater percentage impact on the narrow Ecr band than on the much broader Bcr band.

Table 1. Snow Cover (SC), Surface Snow Albedo (SSA), Difference between clean and measured SSA (D), and Daily Integrated Radiative Forcing (DIRF) values for Bbr and Ecr on the NNTK-1 for dates from temporary analysis (Section 4.2).

Date	SC [%]	SSA [-]					D [-]		DIRF [MJ m^{-2} d^{-1}]	
		Bbr	band3	band4	band1	Ecr	Bbr	Ecr	Bbr	Ecr
06-28-2004	82	0.62	0.65	0.68	0.67	0.63	0.25	0.31	2.46	0.10
06-29-2004	80	0.59	0.56	0.55	0.52	0.47	0.28	0.46	2.53	0.14

Date	SC [%]	SSA [-]					D [-]		DIRF [MJ m^{-2} d^{-1}]	
		Bbr	band3	band4	band1	Ecr	Bbr	Ecr	Bbr	Ecr
08-15-2007	70	0.65	0.74	0.76	0.76	0.74	0.21	0.20	3.32	0.10
08-16-2007	68	0.53	0.55	0.52	0.49	0.45	0.33	0.48	5.36	0.25
08-23-2008	85	0.72	0.75	0.78	0.78	0.72	0.14	0.21	2.61	0.12
08-24-2008	84	0.58	0.72	0.74	0.74	0.67	0.28	0.26	5.17	0.15
07-23-2009	76	0.70	0.68	0.69	0.69	0.66	0.17	0.28	2.08	0.11
07-24-2009	69	0.56	0.68	0.69	0.71	0.68	0.31	0.26	4.09	0.11
08-24-2009	84	0.75	0.83	0.85	0.85	0.77	0.11	0.16	0.99	0.04
08-25-2009	81	0.54	0.71	0.72	0.71	0.64	0.32	0.30	5.79	0.17
06-29-2010	80	0.55	0.58	0.59	0.59	0.56	0.32	0.38	3.19	0.12
06-30-2010	74	0.55	0.51	0.51	0.50	0.45	0.32	0.49	3.19	0.16
07-02-2011	79	0.57	0.62	0.62	0.60	0.57	0.30	0.37	2.70	0.11
07-03-2011	76	0.49	0.48	0.45	0.43	0.39	0.38	0.55	3.64	0.17
08-21-2011	76	0.74	0.80	0.82	0.82	0.78	0.12	0.15	2.21	0.09
08-22-2011	72	0.48	0.60	0.61	0.62	0.59	0.38	0.34	7.07	0.20
08-18-2013	85	0.81	0.72	0.79	0.79	0.73	0.05	0.20	0.90	0.11
08-19-2013	82	0.51	0.56	0.58	0.58	0.53	0.35	0.40	6.01	0.22
08-26-2013	75	0.70	0.76	0.78	0.79	0.77	0.16	0.16	3.03	0.09
08-27-2013	69	0.42	0.50	0.51	0.53	0.52	0.44	0.41	8.31	0.24
07-23-2014	77	0.58	0.55	0.57	0.56	0.54	0.29	0.40	3.21	0.14
07-24-2014	74	0.42	0.47	0.49	0.51	0.49	0.45	0.45	5.27	0.17
08-16-2015	83	0.73	0.82	0.81	0.81	0.74	0.13	0.19	2.19	0.10
08-17-2015	78	0.53	0.67	0.67	0.66	0.61	0.33	0.32	5.73	0.17
06-06-2016	75	0.80	0.83	0.83	0.83	0.78	0.07	0.16	0.69	0.05
06-07-2016	76	0.76	0.72	0.70	0.67	0.61	0.11	0.32	1.11	0.11
08-29-2016	75	0.54	0.55	0.58	0.58	0.55	0.32	0.38	6.24	0.23
08-30-2016	75	0.32	0.38	0.41	0.43	0.40	0.54	0.53	7.42	0.23

4. Conclusions

In this work we used high-quality in-situ measurements of snow surface albedo (SSA) coupled with remote sensing data to make the first estimates of the radiative forcing (RF) over snow in the Chilean Central Andes. We have extended the spectral range of MODDRFS model to wavelengths between 300-2500 nm (Bbr) and obtained a snow reflecting capacity for the NNTK-1 laboratory refuge area, one of the few stations located in the Chilean Andes with capabilities to monitor SSA and related environmental parameters. We focused on isolating the effects of the deposition of BC in snow, which is known to be a key factor influencing SSA variability in the study, by considering the 841-876 nm wavelength range (Ecr). The higher sensitivity of SSA in the Ecr (than in the Bcr) suggests that BC particles (and probably other LAPs) are present in the Andean snowpack impacting snowpack radiation reflection. In the southern area of the UARB, several emission sources of BC can be identified as it is close to Santiago (Chile’s capital and largest city), the international Argentina-Chile route (Paso Los Libertadores) and mining activities (33°08’55’’S, 70°16’53’’W). Overall, we find that reductions in albedo are generally higher than those reported by previous studies in the area using in-situ characterizations, which we attribute to differences in atmospheric contamination that may exist in the different time periods used in the studies and the temporal resolution of the remote sensing data. Nonetheless, the remote sensing MODIS data proved to be a valuable tool for estimating the radiative forcing in regions that are typically inaccessible and improve our understanding of the variability in SSA, which is essential to accurately predict snowmelt and glacier retreat, which in turn control river discharge and freshwater availability in mountain regions.

Author Contributions: Conceptualization, L.F.-V., L.C., R.P.F., T.R.B.-O. and F.C.-B.; methodology, L.F.-V., L.C., R.P.F., T.R.B.-O. and D.P.; software, L.F.-V., T.R.B.-O. and D.P.; validation, L.F.-V., T.R.B.-O. and D.P.; formal

analysis, .F.-V., L.C., R.P.F., T.R.B.-O. and D.P.; investigation, .F.-V., L.C., R.P.F., T.R.B.-O., D.P. and F.C.-B.; resources, L.C., R.P.F., T.R.B.-O. and F.C.-B.; data curation, L.F.-V., T.R.B.-O. and D.P.; writing—original draft preparation, L.F.-V., L.C., R.P.F., T.R.B.-O. and D.P.; visualization, L.F.-V., T.R.B.-O. and D.P.; supervision, L.C., R.P.F., T.R.B.-O. and F.C.-B.; funding acquisition, L.C., R.P.F., T.R.B.-O. and F.C.-B. All authors have read and agreed to the published version of the manuscript.

Funding: This research was funded by the National Research and Development Agency of Chile (ANID), namely, ANID-ANILLO ACT210021, ANID-FONDECYT REGULAR 1221526, ANID-FONDECYT 11220482, ANID-FONDECYT 1231494, and ANID-FONDECYT 3230555 projects.

Data Availability Statement: Data provided on request.

Acknowledgments: We would like to thank the MODIS-NASA, Solar Explorer (Explorador Solar), and NUNATAK-1 laboratory-refuge (CETAM-USM) scientific teams, and their associated personnel for the production of the data used in this research effort.

Conflicts of Interest: The authors declare no conflict of interest.

Appendix A

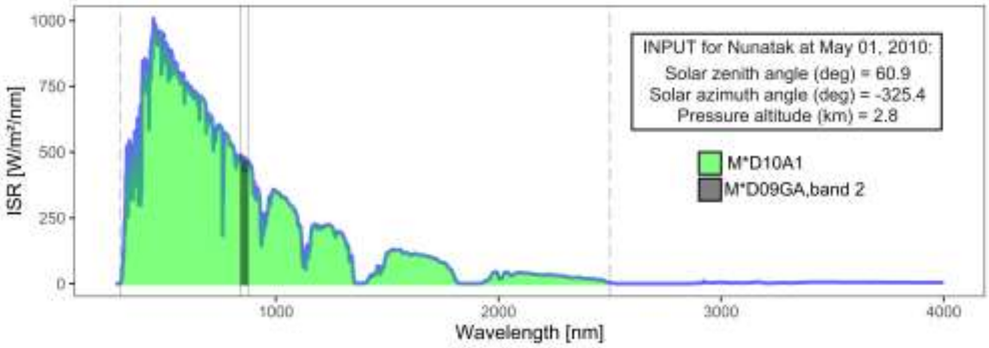

Figure A1. Example of spectral Incident Shortwave Radiation (ISR) in surface in shortwave range model through SBDART for NNTK-1 at 10:00 AM of May 05th, 2010. In green, the spectral range for M*D10A1 (Bbr) and in gray for M*D09GA band 2 (Ecr). The radiation for Bbr and Ecr are equivalent to 99% and 3% respectively regard to Solar Explorer (until to the 4000 nm wavelength) radiation.

Figure A2. Layout of (**A**) MODIS pixel where is located NNTK-1. Also, shows image of (**B**) specific place where is taken records and around NNTK-1.

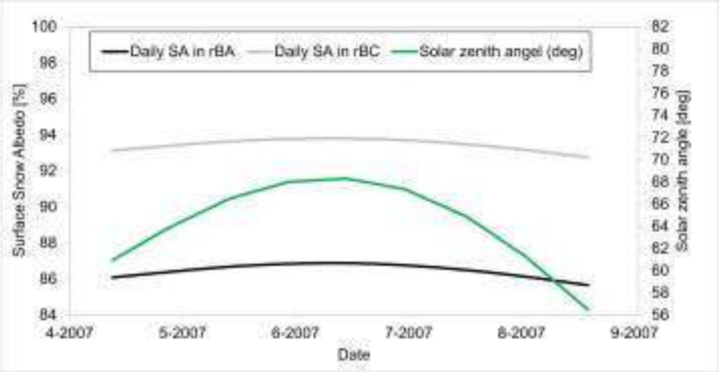

Figure A3. Daily SSAfresh values simulated with SNICAR at 10 AM in the Bbr (black line) and Ecr (gray line), in function of the sza (green line) in NNTK-1, for the months of May to August 2007. Other years have a variation of 1.5 sza degrees which implicates a variation of ±0.001 (included on uncertain mentioned on Section 3.2) on SSA for Bbr and Ecr.

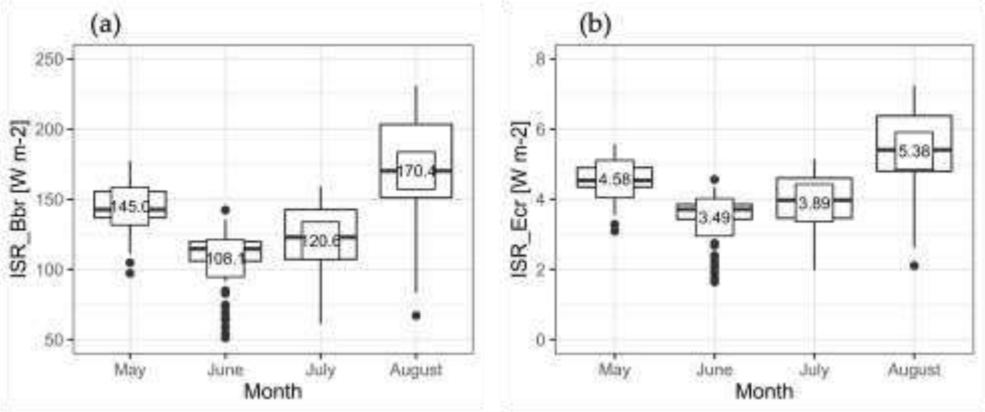

Figure A4. Incident Shortwave Radiation (ISR) in the Bbr (**A**) and Ecr (**B**), grouped by month, for the 2004-2016 period.

References

1. Beres, N.D.; Lapuerta, M.; Cereceda-Balic, F.; Moosmüller, H. Snow Surface Albedo Sensitivity to Black Carbon: Radiative Transfer Modelling. *Atmos.* 2020, *11*.
2. Barry, R.G.; R. Armstrong; T. Callaghan; J. Cherry; S. Gearheard; A. Nolin; D. Russell; C. Zöcler Snow. In Global Outlook for Ice & Snow. **2007**, *UNEP. ISBN*.
3. IPCC *Climate Change 2007: Impacts, Adaptation and Vulnerability: Contribution of Working Group II to the Fourth Assessment Report of the Intergovernmental Panel*; 2007;
4. IPCC Working Group I Contribution to the IPCC Fifth Assessment Report, Climate Change 2013: The Physical Science Basis. *Ipcc* **2013**, *AR5*, 2014.
5. Xu, L.; Dirmeyer, P. Snow - Atmosphere Coupling Strength. Part II: Albedo Effect Versus Hydrological Effect. *J. Hydrometeorol.* **2013**, *14*, 404–418, doi:10.1175/JHM-D-11-0103.1.
6. Gardner, A.S.; Sharp, M.J. A Review of Snow and Ice Albedo and the Development of a New Physically Based Broadband Albedo Parameterization. *J. Geophys. Res. Earth Surf.* 2010, *115*.
7. Beres, N.D.; Sengupta, D.; Samburova, V.; Khlystov, A.Y.; Moosmüller, H. Deposition of Brown Carbon onto Snow: Changes in Snow Optical and Radiative Properties. *Atmos. Chem. Phys.* **2020**, *20*, doi:10.5194/acp-20-6095-2020.
8. Warren, S.G.; Wiscombe, W.J. A Model for the Spectral Albedo of Snow. II: Snow Containing Atmospheric Aerosols. *J. Atmos. Sci.* **1980**, *37*, doi:10.1175/1520-0469(1980)037<2734:AMFTSA>2.0.CO;2.
9. Hadley, O.L.; Kirchstetter, T.W. Black-Carbon Reduction of Snow Albedo. *Nat. Clim. Chang.* **2012**, *2*, 437–440, doi:10.1038/nclimate1433.
10. He, C.; Takano, Y.; Liou, K.N.; Yang, P.; Li, Q.; Chen, F. Impact of Snow Grain Shape and Black Carbon-Snow Internal Mixing on Snow Optical Properties: Parameterizations for Climate Models. *J. Clim.* **2017**, *30*, doi:10.1175/JCLI-D-17-0300.1.

11. Bond, T.C.; Doherty, S.J.; Fahey, D.W.; Forster, P.M.; Berntsen, T.; DeAngelo, B.J.; Flanner, M.G.; Ghan, S.; Kärcher, B.; Koch, D.; et al. Bounding the Role of Black Carbon in the Climate System: A Scientific Assessment. *J. Geophys. Res. Atmos.* **2013**, *118*, 5380–5552, doi:10.1002/jgrd.50171.
12. Skiles, S.M.K.; Painter, T. Daily Evolution in Dust and Black Carbon Content, Snow Grain Size, and Snow Albedo during Snowmelt, Rocky Mountains, Colorado. *J. Glaciol.* **2017**, *63*, doi:10.1017/jog.2016.125.
13. Painter, T.H.; Skiles, S.M.; Deems, J.S.; Bryant, A.C.; Landry, C.C. Dust Radiative Forcing in Snow of the Upper Colorado River Basin: 1. A 6 Year Record of Energy Balance, Radiation, and Dust Concentrations. *Water Resour. Res.* **2012**, *48*, doi:10.1029/2012WR011985.
14. Dang, C.; Warren, S.G.; Fu, Q.; Doherty, S.J.; Sturm, M.; Su, J. Measurements of Light-Absorbing Particles in Snow across the Arctic, North America, and China: Effects on Surface Albedo. *J. Geophys. Res. Atmos.* **2017**, *122*, doi:10.1002/2017JD027070.
15. Skiles, S.M.K.; Flanner, M.; Cook, J.M.; Dumont, M.; Painter, T.H. Radiative Forcing by Light-Absorbing Particles in Snow. *Nat. Clim. Chang.* **2018**, *8*, 964–971, doi:10.1038/s41558-018-0296-5.
16. Hansen, J.; Nazarenko, L. Soot Climate Forcing via Snow and Ice Albedos. *Proc. Natl. Acad. Sci.* **2004**, *101*, 423–428, doi:10.1073/PNAS.2237157100.
17. Bryant, A.; Painter, T.H.; Deems, J.; Bender, S.M. Hydrologic Response to Dust Radiative Forcing in Snow in the Upper Colorado River Basin. *Geophys. Res. Lett.* **2013**, *40*, doi:10.1002/grl.50773.
18. Jacobi, H.W.; Lim, S.; Ménégoz, M.; Ginot, P.; Laj, P.; Bonasoni, P.; Stocchi, P.; Marinoni, A.; Arnaud, Y. Black Carbon in Snow in the Upper Himalayan Khumbu Valley, Nepal: Observations and Modeling of the Impact on Snow Albedo, Melting, and Radiative Forcing. *Cryosphere* **2015**, *9*, doi:10.5194/tc-9-1685-2015.
19. Santra, S.; Verma, S.; Fujita, K.; Chakraborty, I.; Boucher, O.; Takemura, T.; Burkhart, J.F.; Matt, F.; Sharma, M. Simulations of Black Carbon (BC) Aerosol Impact over Hindu Kush Himalayan Sites: Validation, Sources, and Implications on Glacier Runoff. *Atmos. Chem. Phys.* **2019**, *19*, doi:10.5194/acp-19-2441-2019.
20. Petzold, A.; Ogren, J.A.; Fiebig, M.; Laj, P.; Li, S.M.; Baltensperger, U.; Holzer-Popp, T.; Kinne, S.; Pappalardo, G.; Sugimoto, N.; et al. Recommendations for Reporting Black Carbon Measurements. *Atmos. Chem. Phys.* **2013**, *13*, doi:10.5194/acp-13-8365-2013.
21. Lapuerta, M.; González-Correa, S.; Ballesteros, R.; Cereceda-Balic, F.; Moosmüller, H. Albedo Reduction for Snow Surfaces Contaminated with Soot Aerosols: Comparison of Experimental Results and Models. *Aerosol Sci. Technol.* **2022**, *56*, 847–858, doi:10.1080/02786826.2022.2091975.
22. Lee, W.L.; Liou, K.N.; He, C.; Liang, H.C.; Wang, T.C.; Li, Q.; Liu, Z.; Yue, Q. Impact of Absorbing Aerosol Deposition on Snow Albedo Reduction over the Southern Tibetan Plateau Based on Satellite Observations. *Theor. Appl. Climatol.* **2017**, *129*, doi:10.1007/s00704-016-1860-4.
23. Zhong, X.; Kang, S.; Zhang, W.; Yang, J.; Li, X.; Zhang, Y.; Liu, Y.; Chen, P. Light-Absorbing Impurities in Snow Cover across Northern Xinjiang, China. *J. Glaciol.* **2019**, *65*, doi:10.1017/jog.2019.69.
24. Saleh, R.; Robinson, E.S.; Tkacik, D.S.; Ahern, A.T.; Liu, S.; Aiken, A.C.; Sullivan, R.C.; Presto, A.A.; Dubey, M.K.; Yokelson, R.J.; et al. Brownness of Organics in Aerosols from Biomass Burning Linked to Their Black Carbon Content. *Nat. Geosci.* **2014**, *7*, 647–650, doi:10.1038/ngeo2220.
25. Brown, H.; Wang, H.; Flanner, M.; Liu, X.; Singh, B.; Zhang, R.; Yang, Y.; Wu, M. Brown Carbon Fuel and Emission Source Attributions to Global Snow Darkening Effect. *J. Adv. Model. Earth Syst.* **2022**, *14*, doi:10.1029/2021MS002768.
26. Moosmüller, H.; Chakrabarty, R.K.; Arnott, W.P. Aerosol Light Absorption and Its Measurement: A Review. *J. Quant. Spectrosc. Radiat. Transf.* 2009, *110*.
27. Cereceda-Balic, F.; Ruggeri, M.F.; Vidal, V.; Ruiz, L.; Fu, J.S. Understanding the Role of Anthropogenic Emissions in Glaciers Retreat in the Central Andes of Chile. *Environ. Res.* **2022**, 113756, doi:https://doi.org/10.1016/j.envres.2022.113756.
28. Painter, T.H.; Deems, J.S.; Belnap, J.; Hamlet, A.F.; Landry, C.C.; Udall, B. Response of Colorado River Runoff to Dust Radiative Forcing in Snow. *Proc. Natl. Acad. Sci.* **2010**, *107*, doi:10.1073/pnas.0913139107.
29. Di Mauro, B.; Garzonio, R.; Rossini, M.; Filippa, G.; Pogliotti, P.; Galvagno, M.; Morra Di Cella, U.; Migliavacca, M.; Baccolo, G.; Clemenza, M.; et al. Saharan Dust Events in the European Alps: Role in Snowmelt and Geochemical Characterization. *Cryosphere* **2019**, *13*, doi:10.5194/tc-13-1147-2019.
30. Bolaño-Ortiz, T.R.; Pascual-Flores, R.M.; López-Noreña, A.I.; Ruggeri, M.F.; Lakkis, S.G.; Fernández, R.P.; Puliafito, S.E. Assessment of Absorbing Aerosols on Austral Spring Snow Albedo Reduction by Several Basins in the Central Andes of Chile from Daily Satellite Observations (2000–2016) and a Case Study with the WRF-Chem Model. *SN Appl. Sci.* **2019**, *1*, 1352, doi:10.1007/s42452-019-1256-z.
31. Cordero, R.R.; Sepúlveda, E.; Feron, S.; Wang, C.; Damiani, A.; Fernandoy, F.; Neshyba, S.; Rowe, P.M.; Asencio, V.; Carrasco, J.; et al. Black Carbon in the Southern Andean Snowpack. *Environ. Res. Lett.* **2022**, *17*, doi:10.1088/1748-9326/ac5df0.
32. Cereceda-Balic, F.; Vidal, V.; Moosmüller, H.; Lapuerta, M. Reduction of Snow Albedo from Vehicle Emissions at Portillo, Chile. *Cold Reg. Sci. Technol.* **2018**, *146*, 43–52, doi:10.1016/J.COLDREGIONS.2017.11.008.

33. Rowe, P.M.; Cordero, R.R.; Warren, S.G.; Stewart, E.; Doherty, S.J.; Pankow, A.; Schrempf, M.; Casassa, G.; Carrasco, J.; Pizarro, J.; et al. Black Carbon and Other Light-Absorbing Impurities in Snow in the Chilean Andes. *Sci. Rep.* **2019**, *9*, 1–16, doi:10.1038/s41598-019-39312-0.
34. Malmros, J.K.; Mernild, S.H.; Wilson, R.; Tagesson, T.; Fensholt, R. Snow Cover and Snow Albedo Changes in the Central Andes of Chile and Argentina from Daily MODIS Observations (2000–2016). *Remote Sens. Environ.* **2018**, *209*, 240–252, doi:10.1016/J.RSE.2018.02.072.
35. Pu, W.; Cui, J.; Shi, T.; Zhang, X.; He, C.; Wang, X. The Remote Sensing of Radiative Forcing by Light-Absorbing Particles (LAPs) in Seasonal Snow over Northeastern China. *Atmos. Chem. Phys.* **2019**, *19*, doi:10.5194/acp-19-9949-2019.
36. Dowson, A.J.; Sirguey, P.; Cullen, N.J. Variability in Glacier Albedo and Links to Annual Mass Balance for the Gardens of Eden and Allah, Southern Alps, New Zealand. *Cryosphere* **2020**, *14*, doi:10.5194/tc-14-3425-2020.
37. Molina, L.T.; Andrade, M.; Baumgardner, D.; Casassa, G.; Dawidowski, L.; Garreaud, R.; Huneeus, N.; Lambert, F. Pollution and Its Impacts on the South American Cryosphere. *Earth's Futur.* **2015**, *3*, 1–26, doi:https://doi.org/10.1002/2015EF000311.
38. Sharma, S.; Richard Leaitch, W.; Huang, L.; Veber, D.; Kolonjari, F.; Zhang, W.; Hanna, S.J.; Bertram, A.K.; Ogren, J.A. An Evaluation of Three Methods for Measuring Black Carbon in Alert, Canada. *Atmos. Chem. Phys.* **2017**, *17*, doi:10.5194/acp-17-15225-2017.
39. Painter, T.H.; Bryant, A.C.; Skiles, S.M. Radiative Forcing by Light Absorbing Impurities in Snow from MODIS Surface Reflectance Data. *Geophys. Res. Lett.* **2012**, *39*, n/a-n/a, doi:10.1029/2012GL052457.
40. Miller, S.D.; Wang, F.; Burgess, A.B.; McKenzie Skiles, S.; Rogers, M.; Painter, T.H. Satellite-Based Estimation of Temporally Resolved Dust Radiative Forcing in Snow Cover. *J. Hydrometeorol.* **2016**, *17*, 1999–2011, doi:10.1175/JHM-D-15-0150.1.
41. Bown, F.; Rivera, A.; Acuña, C. Recent Glacier Variations at the Aconcagua Basin, Central Chilean Andes. In Proceedings of the Annals of Glaciology; 2008; Vol. 48.
42. Falvey, M.; Garreaud, R.D. Wintertime Precipitation Episodes in Central Chile: Associated Meteorological Conditions and Orographic Influences. *172 J. Hydrometeorol.* **2007**, *8*, 171–193, doi:10.1175/JHM562.1.
43. Garreaud, R.D.; Boisier, J.P.; Rondanelli, R.; Montecinos, A.; Veloso-aguila, H.H.S.D. The Central Chile Mega Drought (2010 – 2018): A Climate Dynamics Perspective. **2020**, 421–439, doi:10.1002/joc.6219.
44. Saavedra, F.A.; Kampf, S.K.; Fassnacht, S.R.; Sibold, J.S. Changes in Andes Snow Cover from MODIS Data, 2000–2016. *Cryosph.* **2018**, *12*, 1027–1046, doi:10.5194/tc-12-1027-2018.
45. Dussaillant, I.; Berthier, E.; Brun, F.; Masiokas, M.; Hugonnet, R.; Favier, V.; Rabatel, A.; Pitte, P.; Ruiz, L. Two Decades of Glacier Mass Loss along the Andes. *Nat. Geosci.* **2019**, *12*, 802–808, doi:10.1038/s41561-019-0432-5.
46. Cereceda-Balic, F.; Vidal, V.; Moosmüller, H.; Lapuerta, M. One-Year Long Time Atmospheric Monitoring Data, Snow Albedo and BC in Snow Measurement in Portillo, Los Andes, Chile. In Proceedings of the Proceedings of the Air and Waste Management Association's Annual Conference and Exhibition, AWMA; Air and Waste Management Association, 2019; Vol. 2019-June.
47. Hall, D.K.; Riggs, G.A.; Salomonson, V. V; DiGirolamo, N.E.; Bayr, K.J. MODIS Snow-Cover Products. *Remote Sens. Environ.* **2002**, *83*, 181–194.
48. Jing, J.; Wu, Y.; Tao, J.; Che, H.; Xia, X.; Zhang, X.; Yan, P.; Zhao, D.; Zhang, L. Observation and Analysis of Near-Surface Atmospheric Aerosol Optical Properties in Urban Beijing. *Particuology* **2015**, *18*, doi:10.1016/j.partic.2014.03.013.
49. Molina, A.; Falvey, M.; Rondanelli, R. A Solar Radiation Database for Chile. *Sci. Rep.* **2017**, *7*, doi:10.1038/s41598-017-13761-x.
50. Chou, M.-D.; Suarez, M. A Solar Radiation Parameterization (CLIRAD-SW) for Atmospheric Studies. *NASA Tech. Memo* **1999**, *10460*.
51. Kopp, G.; Lawrence, G.; Rottman, G. The Total Irradiance Monitor (TIM): Science Results. *Sol. Phys.* 2005, *230*.
52. Van Zyl, J.J. The Shuttle Radar Topography Mission (SRTM): A Breakthrough in Remote Sensing of Topography. In Proceedings of the Acta Astronautica; 2001; Vol. 48.
53. Mukul, M.; Srivastava, V.; Jade, S.; Mukul, M. Uncertainties in the Shuttle Radar Topography Mission (SRTM) Heights: Insights from the Indian Himalaya and Peninsula. *Sci. Rep.* **2017**, *7*, doi:10.1038/srep41672.
54. Hillger, D.W.; Schmit, T.J. Observing Systems: The GOES-13 Science Test: A Synopsis. *Bull. Am. Meteorol. Soc.* **2009**, *90*, 592–597, doi:10.1175/2008BAMS2564.1.
55. Flanner, M.G.; Arnheim, J.B.; Cook, J.M.; Dang, C.; He, C.; Huang, X.; Singh, D.; Skiles, S.M.; Whicker, C.A.; Zender, C.S. SNICAR-ADv3: A Community Tool for Modeling Spectral Snow Albedo. *Geosci. Model Dev.* **2021**, *14*, 7673–7704, doi:10.5194/gmd-14-7673-2021.
56. Ricchiazzi, P.; Yang, S.; Gautier, C.; Sowle, D. SBDART: A Research and Teaching Software Tool for Plane-Parallel Radiative Transfer in the Earth's Atmosphere. *Bull. Am. Meteorol. Soc.* **1998**, *79*, doi:10.1175/1520-0477(1998)079<2101:SARATS>2.0.CO;2.

57. Obregón, M.A.; Serrano, A.; Costa, M.J.; Silva, A.M. Validation of LibRadtran and SBDART Models under Different Aerosol Conditions. In Proceedings of the IOP Conference Series: Earth and Environmental Science; 2015; Vol. 28.
58. Fu, Y.; Zhu, J.; Yang, Y.; Yuan, R.; Liu, G.; Xian, T.; Liu, P. Grid-Cell Aerosol Direct Shortwave Radiative Forcing Calculated Using the SBDART Model with MODIS and AERONET Observations: An Application in Winter and Summer in Eastern China. *Adv. Atmos. Sci.* **2017**, *34*, doi:10.1007/s00376-017-6226-z.
59. Flanner, M.G.; Zender, C.S.; Randerson, J.T.; Rasch, P.J. Present-Day Climate Forcing and Response from Black Carbon in Snow. *J. Geophys. Res.* **2007**, *112*, D11202, doi:10.1029/2006JD008003.
60. Dang, C.; Fu, Q.; Warren, S.G. Effect of Snow Grain Shape on Snow Albedo. *J. Atmos. Sci.* **2016**, *73*, doi:10.1175/JAS-D-15-0276.1.
61. Cornwell, E.; Molotch, N.P.; McPhee, J. Spatio-Temporal Variability of Snow Water Equivalent in the Extra-Tropical Andes Cordillera from Distributed Energy Balance Modeling and Remotely Sensed Snow Cover. *Hydrol. Earth Syst. Sci.* **2016**, *20*, doi:10.5194/hess-20-411-2016.
62. Picard, G.; Libois, Q.; Arnaud, L. Refinement of the Ice Absorption Spectrum in the Visible Using Radiance Profile Measurements in Antarctic Snow. *Cryosphere* **2016**, *10*, 2655–2672, doi:10.5194/tc-10-2655-2016.
63. Cereceda-Balic, F.; Vidal, V.; Ruggeri, M.F.; González, H.E. Black Carbon Pollution in Snow and Its Impact on Albedo near the Chilean Stations on the Antarctic Peninsula: First Results. *Sci. Total Environ.* **2020**, *743*, doi:10.1016/j.scitotenv.2020.140801.
64. Cui, J.; Shi, T.; Zhou, Y.; Wu, D.; Wang, X.; Pu, W. Satellite-Based Radiative Forcing by Light-Absorbing Particles in Snow across the Northern Hemisphere. *Atmos. Chem. Phys.* **2021**, *21*, doi:10.5194/acp-21-269-2021.
65. Warren, S.G. Optical Properties of Snow. *Rev. Geophys.* **1982**, *20*, 67–89, doi:https://doi.org/10.1029/RG020i001p00067.
66. Panicker, A.S.; Sandeep, K.; Gautam, A.S.; Trimbake, H.K.; Nainwal, H.C.; Beig, G.; Bisht, D.S.; Das, S. Black Carbon over a Central Himalayan Glacier (Satopanth): Pathways and Direct Radiative Impacts. *Sci. Total Environ.* **2021**, *766*, doi:10.1016/j.scitotenv.2020.144242.